Progress In Electromagnetics Research C, Vol. 154, 1–9, 2025 PIER C

(Received 25 January 2025, Accepted 7 March 2025, Scheduled 19 March 2025)

Design and Analysis of a Novel Segmented Secondary Modular Double-Sided Flux-Switching Linear Motor

Yuxiao Zhu[1,2], Yongkuan Li[1,2], Yujian Chang[1,2,*], Jiaming Li[1,2], and Jin Chen[3]

[1]*Hebei Provincial Collaborative Innovation Center of Transportation Power Grid Intelligent Integration Technology and Equipment, Shijiazhuang Tiedao University, Shijiazhuang, Hebei 050043, China*
[2]*School of Electrical and Electronics Engineering, Shijiazhuang Tiedao University, Hebei 050043, China*
[3]*Hebei Kunneng Electric Power Engineering Consulting Co., Ltd., Hebei 050000, China*

ABSTRACT: In this paper, a novel double-sided flux-switching linear motor is proposed. The motor adopts the structure of primary modularization and secondary segment. It has the advantages of high safety, high thrust density, and low thrust fluctuation. In this paper, the detent force characteristics of the proposed motor are analyzed, and the influence of the end effect on the magnetic congregate effect is discussed, which has reference value for the study of the permanent magnet linear motor with transverse magnetization. Moreover, according to the above analysis, suitable and effective structural optimization and parameter optimization methods are designed for the motor. After the optimization, the proposed motor achieves higher thrust output and significantly lower fluctuation. Finally, a prototype is constructed for validation.

1. INTRODUCTION

The advancement of industrialization and urbanization has led to increased demands for linear traction applications. Traditional rotary motors, relying on transmission systems, face challenges in meeting diverse application requirements. In contrast, linear motors, which eliminate the need for a transmission mechanism, exhibit superior starting, acceleration, and braking performance, thus presenting distinct advantages in the field of traction [1, 2]. The flux-switching linear motor, a novel type of magnetic field modulation motor [3] known for its high efficiency and excellent thrust density [4–6], has garnered significant attention from scholars. It is widely regarded as the most promising direction for the development of linear traction motors due to its consideration of electromagnetic effects and cost-effectiveness in construction. The flux-switching linear motor has been extensively researched across diverse fields such as precision lathes, urban intelligent elevators, and rail transportation [7].

In [8], finite element analysis was employed to optimize the parameters of a flux-switched linear motor utilized in rail transit, and a single-side flux-switched linear motor model with excellent performance for rail transit was obtained. By comparing parameters such as thrust, efficiency, and construction cost with those of the operational metro's linear induction motor, it was demonstrated that the application of flux-switched linear motors in rail transit is viable. Ref. [9] focused on optimizing the motor structure of flux-switching motors by proposing a new module structure. The findings indicate that modular linear motors can significantly enhance thrust performance, alleviate end effects, and enhance motor reliability compared to traditional linear motors. In [10], a secondary segmented single-side flux-switched linear motor was introduced; this segmented secondary structure offers new insights into designing and researching flux-switched motors. The single-sided permanent magnet linear motors have been extensively studied but are plagued by a common disadvantage — high normal force. To address this challenge and adapt to more application scenarios, scholars have proposed double-side linear motors [11].

The double-sided structure has evolved from the single-sided linear motor and is widely regarded as the optimal solution for reducing the normal force. In [12], a modular thin yoke flux-switched permanent magnet linear motor was designed for elevator applications, along with its corresponding control system. The design scheme of the modular thin yoke has significantly influenced the design of double-side linear motors. Additionally, in [13], a double-side flux-switching linear motor for rail transit was proposed, and its parameters were optimized using a neural network algorithm to achieve optimal thrust performance. Furthermore, [14] introduced a secondary segmented double-side linear motor that achieved very high thrust density and proposed schemes to reduce thrust fluctuation; however, even after optimization, the thrust fluctuation remained at a high level.

Despite extensive research in this field, the issue of high thrust fluctuation in double-side flux-switched linear motors remains unresolved. To solve this problem, this paper proposes a novel type of segmented secondary modular double-sided flux-switching linear motor based on the principle of flux-switching. This innovative motor adopts a new modular primary structure that effectively reduces thrust fluctuation by minimizing detent force. The sections are organized as follows. Section 2 describes the structure and operation mechanism of the pro-

---

* Corresponding author: Yujian Chang (changyj@stdu.edu.cn).

doi:10.2528/PIERC25012502

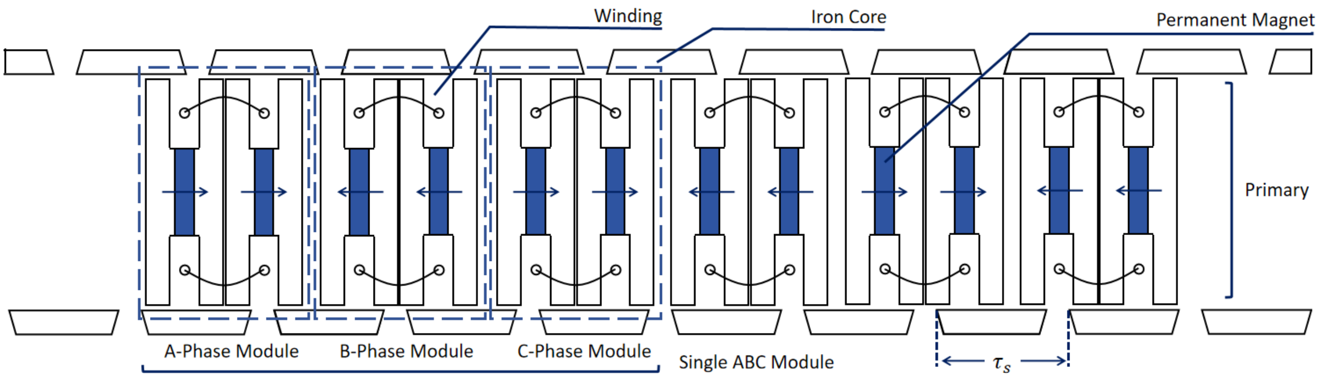

FIGURE 1. Motor structure.

posed motor and presents a finite element model. Section 3 analyzes detent force characteristics and proposes structural optimization schemes; subsequently, parameter optimization is conducted to obtain optimal motor parameters which are compared with existing models to demonstrate superior thrust performance. Section 4 involves building a prototype to verify no-load back electromotive force (EMF) characteristics and validate both motor design correctness and simulation. Finally, the conclusion is drawn in Section 5.

2. MOTOR DESIGN

2.1. Motor Design Principle and Motor Structure

According to the existing model of flux-switching linear motor, the following design principles are summarized:

(1) Primary modularity is advantageous for mitigating end effects, reducing inter-module adverse interaction, and enhancing motor operation safety [9].

(2) Proper adjustment of spacing between primary modules enables mutual cancellation of detent forces, thereby minimizing thrust fluctuations [9].

(3) Segmenting the secondary simplifies the magnetic circuit and significantly reduces the occupied area of the secondary part [10, 11].

(4) Appropriate dislocation of the two secondary stators can strengthen the air gap magnetic field and thrust while diminishing thrust fluctuations [12].

Under the guidance of the above design principles and based on the principle of flux-switching [3, 7], a new structure of flux-switching linear motor is proposed in this paper to achieve lower thrust fluctuation. This motor has a novel modular structure, which is completely different from the existing structure. Fig. 1 illustrates the overall structure. The motor consists of a primary and two secondary. The secondary is fixed, and the primary moves in a straight line between the two secondary. The secondary is composed of segmented iron cores, and the distance between adjacent iron cores is the secondary pole distance, denoted as τ_s. There is a $\tau_s/2$ horizontal position gap between the upper and lower secondary. This plays an important role in realizing the principle of magnetic flux switching and minimizing thrust fluctuations. The primary comprises six individual modules with each divided into two sub-modules. Each sub-module contains two iron cores sandwiched by transversely magnetized permanent magnets. The magnetizing direction of the permanent magnet is shown by the arrow in Fig. 1. Two windings with matching directions are installed on both the upper and lower sides of each pair of permanent magnets within every sub-module. The six modules supply three-phase current alternately, with spacing between individual modules set at $(n \pm 1/6)\tau_s$ or $(n \pm 1/3)\tau_s$ (n is an arbitrary integer, and τ_s represents the secondary pole distance). This ensures that there is a phase difference equivalent to 1/3 or 1/6 secondary pole distance between adjacent modules to facilitate the generation of no-load back EMF corresponding to the three-phase current phase, while the time to run through a secondary pole distance τ_s corresponds to an electrical period T.

2.2. Principle of Operation

The proposed secondary segmented flux-switched linear motor operates based on the principle of flux-switching [15–17] as illustrated in Fig. 2. In position (a), the left permanent magnet and lower segmented iron core create a closed magnetic circuit with minimal reluctance, while the right permanent magnet and upper segmented iron core form another closed magnetic circuit, resulting in maximum forward magnetic flux in

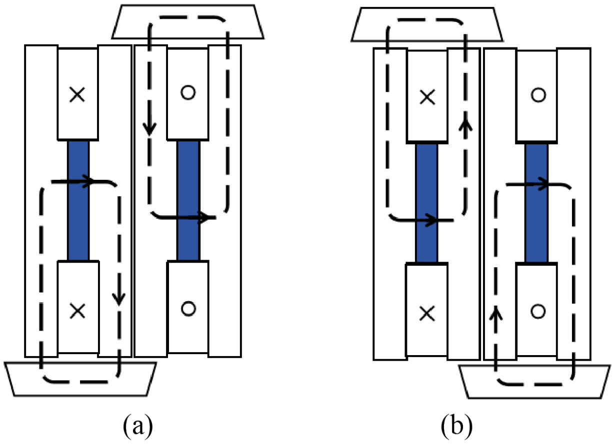
(a)
(b)

FIGURE 2. Diagram of the principle of flux-switching. (a) Forward magnetic flux, (b) reverse magnetic flux.

the winding. When in position (b), the left permanent magnet and upper segmented iron core form a closed magnetic circuit, and similarly, the right permanent magnet and lower segmented iron core form another closed magnetic circuit, leading to maximum reverse magnetic flux in the winding. It is evident that as the secondary moves, it switches between position (a) and position (b) relative to the primary, creating an alternating magnetic circuit within the winding which generates back electromotive force. The no-load back EMF is zero at positions (a) and (b) and peaks at their midpoint.

The motor proposed in this paper operates on the flux-switching principle, which is consistent with the conventional flux-switched motor. On the premise of linear simplification of magnetic circuit, the simplified equation of motor thrust derived by magnetic coenergy method is shown in Equation (1). Please refer to [18] for detailed derivation.

$$F_e = \frac{dW}{dx} = \frac{d}{dx}\left[\frac{1}{2}\boldsymbol{I}^T\boldsymbol{L}\boldsymbol{I} + \boldsymbol{\varphi}_{pm}^T\boldsymbol{I}\right] + F_{cog} \tag{1}$$

where x represents the actuator displacement, φ_{pm} the permanent magnet flux vector, $\boldsymbol{I}$ the current vector, $\boldsymbol{L}$ the inductance matrix, and F_{cog} the detent force.

2.3. The Finite Element Analysis

Under the design principle outlined in Section 2, the initial finite element model of the motor is constructed according to the labels in Fig. 3 and the data in Table 1.

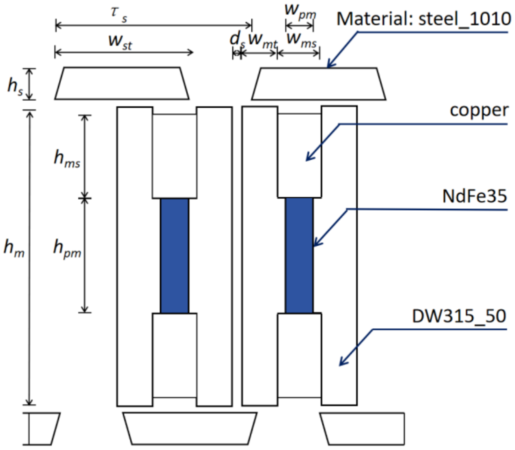

FIGURE 3. Diagram of the motor module.

The permanent magnets in the flux-switched motor typically utilize an arrangement of alternating magnetic poles [21]. This arrangement can achieve a higher air gap magnetic density. In this paper, the permanent magnet alternating arrangement is also adopted. The thrust performance calculated according to the finite element model is shown in Fig. 4.

As shown in Fig. 4, the average thrust is 782.9 N, and the thrust fluctuation is 159.8 N. The initial motor model has a high thrust fluctuation. Thrust fluctuation is an important index to measure motor performance, and the initial motor model will be optimized to solve this problem.

TABLE 1. Main parameters.

Items	Specifications
Primary iron core width, w (mm)	150
Air gap length, g (mm)	0.8
PM height, h_{pm} (mm)	16
Primary height, h_m (mm)	50
Primary tooth width, w_{mt} (mm)	6.1
Primary slot width, w_{ms} (mm)	8.5
PM width, w_{pm} (mm)	6.1
distance between segments, d_s (mm)	1
Secondary pole pitch, τ_s (mm)	35
Secondary tooth width, w_{st} (mm)	28
Secondary height, h_s (mm)	6.5
Rated speed, v (m/s)	0.5
Turns of coils per slot, N	53
Rated current, I (A)	15

3. MOTOR OPTIMIZATION

3.1. Detent Force Analysis

As shown in Fig. 4, thrust fluctuation is mainly generated by detent force, which is consistent with a large number of studies on double-sided motors [14, 21]. This paper will reduce thrust fluctuation by reducing detent force.

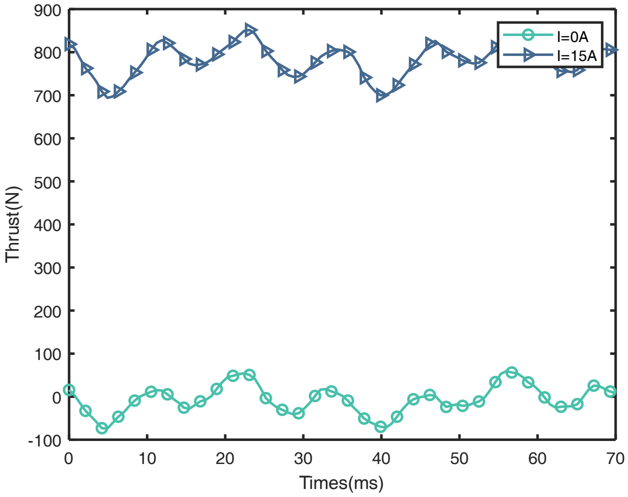

FIGURE 4. Thrust.

In order to study the causes of high detent force fluctuation, the detent force of a single ABC module and the whole motor (including two ABC modules) were compared and analyzed in this paper. The thrust curve and fast Fourier transform (FFT) results are shown in Fig. 5.

It can be seen from Fig. 5 that the main harmonic order of the detent force of the single ABC module and the whole motor (including two single ABC modules) is 2nd and 6th, of which the 6th-order components have a relatively obvious superposition relationship, and the amplitude of the 2nd-order components is basically the same.

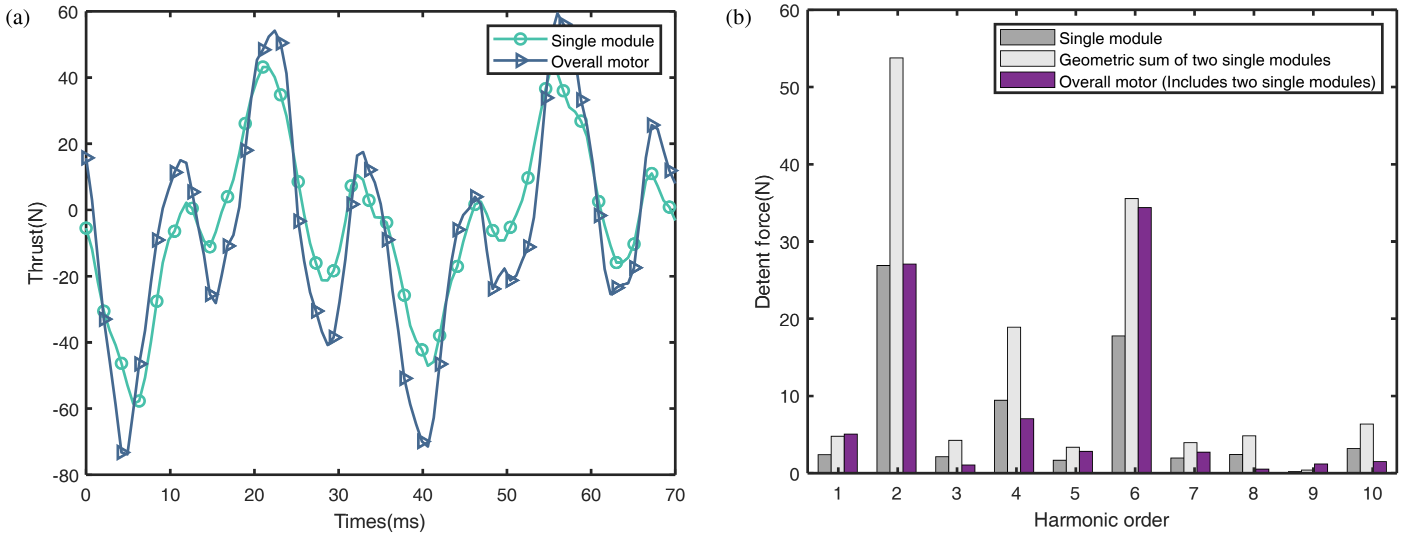

FIGURE 5. Detent force. (a) Detent force, (b) FFT of detent force.

This is an interesting result. It is usually thought that each module operates independently, and the time phase of the two modules is the same, so the 2nd order detent force of the whole motor should also be geometric sum of two single modules, just like the 6th order detent force in Fig. 5. However, this is not the case, so we speculate that the magnetic congregate effect between the two ABC modules affects the superposition of the 2nd-order detent forces of the two modules. The following paragraphs of this section will analyze the causes of the above 2nd order detent force in detail.

In this section, the single ABC module with the permanent magnet in the same direction (NNN) is set up for comparative analysis to study the influence of the concentrated magnetic effect on the detent force. Maxwell stress tensor method was used for analysis [22–25].

The motor thrust expression under the same direction arrangement (NNN) can be seen in Equation (2).

$$F_{NNN}(t) = \frac{w}{\mu_0}\oint_L B_n(t)B_t(t)dL \tag{2}$$

where t represents the time, w the motor width, μ_0 the air permeability, L the motor length, and B_n and B_t represent the normal and tangential magnetic densities of the air gap

The permanent magnet alternating arrangement (NSN) can be achieved by reversing the direction of module B's permanent magnet arrangement in NNN arrangement. Therefore, based on B_n and B_t, the corresponding air gap magnetic density of module B should be replaced by the negative value of the original air gap magnetic density B. The change in air gap magnetic density caused by accumulated magnetic effects is denoted as ΔB.

The expression for motor thrust under the permanent magnet alternating arrangement (NSN) is shown in Equation (3).

$$F_{NSN}(t) = \frac{w}{\mu_0}\oint_L (B_n(t)+\Delta B_n(t))\cdot(B_t(t)+\Delta B_t(t))dL \tag{3}$$

By subtracting Equation (2) from Equation (3), it is deduced that the detent force produced by magnetic congregate effect can be calculated by Equation (4).

$$F_{\Delta}(t) = \frac{w}{\mu_0}\oint_l (\Delta B_n(t)B_t(t) + \Delta B_t(t)B_n(t) + \Delta B_t(t)\Delta B_n(t))dl \tag{4}$$

where l denotes the length of the motor involved in generating the magnetic aggregation effect of the detent force.

According to Formula (4), the detent force generated by the magnetic congregate effect between module A and module B and the detent force generated by the magnetic congregate effect between module B and module C can be calculated respectively, as shown in Fig. 6. The FFT results of Fig. 6 are shown in Fig. 7.

It can be seen that the concentrated magnetic effect will produce a significant 2nd-order detent force component. The motor proposed in this paper has six modules, and the transverse-arranged permanent magnets installed in adjacent modules have opposite magnetic directions, that is, there are five magnetizing positions in the motor, as shown in Fig. 8(a). The phase difference of the detent force generated by the magnetic congregate effect in the time phase is 1/3 electrical period and 2/3 electrical period for the 2nd-order harmonic. The detent force generated by the concentrated magnetic effect at position 1 is denoted as detent force 1, and the other positions are the same. The time vector diagram is shown in Fig. 8(b). Therefore, the direction of the resultant detent force generated by the five concentrated magnetic effect positions of the whole motor is the same as the detent force 3, and the phase is opposite. Under a single ABC module, there exists a concentrated magnetic effect at positions 1 and 2, which also synthesizes detent forces of equal amplitude in reverse with that of detent force 3. Therefore, the amplitude of the 2nd-order detent forces of the single ABC module and the whole motor in Fig. 5 are similar.

The rotating motor has a sixth magnetic congregate position between module A on the left and module C on the right, which

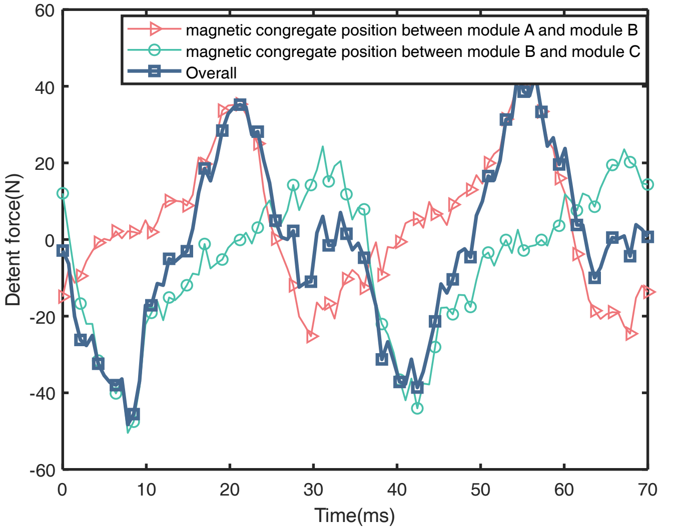

FIGURE 6. The detent force generated by the magnetic congregate effect.

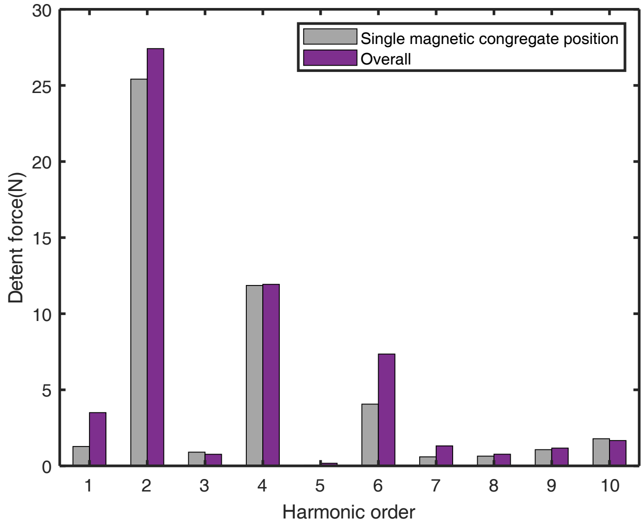

FIGURE 7. The FFT of the generated detent force.

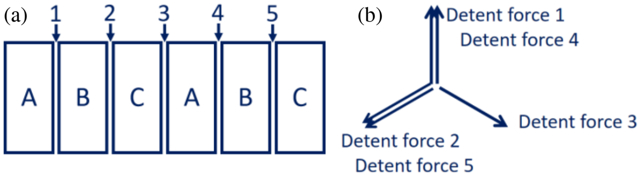

FIGURE 8. Schematic diagram of detent force generated by the magnetic congregate effect. (a) Concentrated magnetic effect position. (b) The time vector diagram.

makes the detent forces generated by the six magnetic congregate positions cancel each other out. It can be seen that although the primary modularization can reduce the end effect caused by the different end reluctance, the asymmetric magnetic congregate effect of permanent magnets caused by the linear structure also brings obvious end effect. This finding has reference value for the design of other types of permanent magnet linear motors.

To solve this problem, this paper will reduce the spacing between two ABC modules appropriately to increase the magnetic congregate effect between the two ABC modules to offset the detent force caused by the magnetic congregate effect.

Corresponding to Fig. 8, reinforce the 3rd branches for better offset. The implementation of motor structure optimization will be analyzed in the next section.

3.2. Motor Structure Optimization

It is evident from Fig. 5 that, in addition to the second-order detent force harmonic caused by the magnetic congregate effect, the fourth and sixth-order primary fluctuations are also present in both modules. Due to the higher amplitude and shorter cycle length of the sixth-order detent force, subsequent optimization primarily focuses on this harmonic: We move the left ABC module $\tau_s/24$ to the right and the right ABC module $\tau_s/24$ to the left, and the initial phase of the input current remains unchanged, as shown in Fig. 9. Consequently, there is a separation of the electrical phase between the left and right parts by $\tau_s/12$, resulting in a $T/2$ displacement in the 6th-order detent forces generated by these modules. The optimized detent forces for each module individually and their overall detent forces are depicted in Fig. 10. It can be observed that this optimization scheme yields excellent results, leading to an obvious offset phenomenon in detent forces between the left and right modules. On the other hand, due to the enhancement of the magnetic congregate effect between the two ABC modules, the 2nd-order detent force is also reduced well. As a result of these structure optimizations, a successful reduction of detent forces for the proposed motor has been achieved.

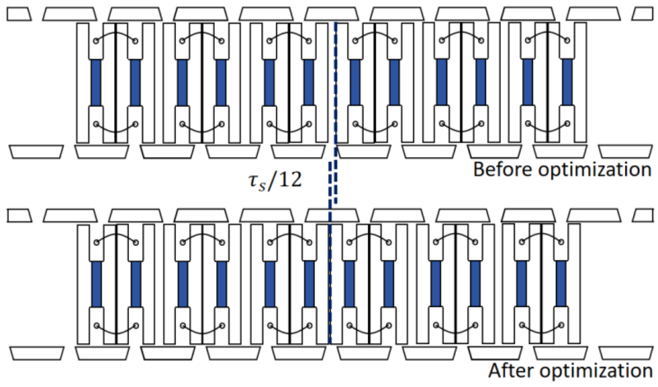

FIGURE 9. Structure optimization diagram.

The thrust at the armature current of 15 A is calculated as shown in Fig. 11.

It is clear from Fig. 11 that this optimization scheme has played a significant role. Thrust fluctuation decreased from 160 N to 46 N, and the average thrust value decreased from 783 N to 767 N. The mean thrust is slightly reduced, but the thrust fluctuation is significantly reduced.

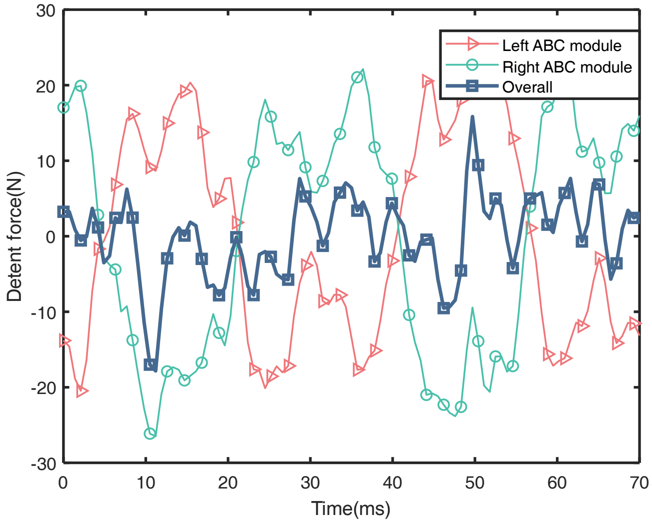

FIGURE 10. Detent force offset diagram.

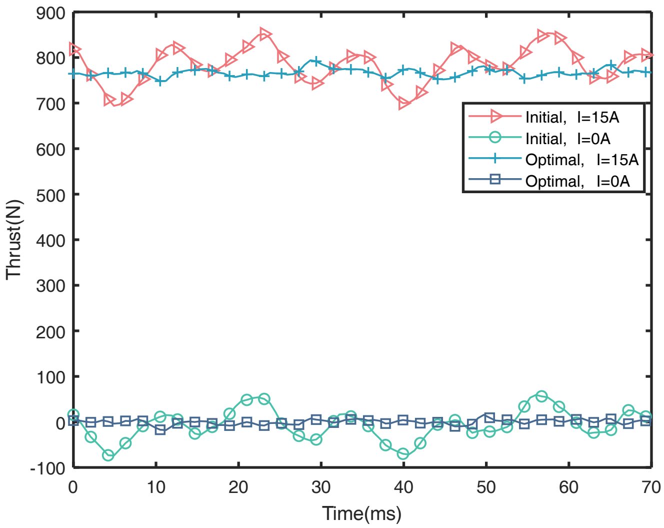

FIGURE 11. Comparison of motor thrust before and after structure optimization.

3.3. Motor Parameter Optimization

To improve the electromagnetic performance, the main parameters of the initially designed motor were optimized. The key optimization parameters include primary tooth width w_{mt}, secondary pole pitch w_{st}, and secondary height, h_s. The optimization objective is greater thrust and smaller thrust fluctuation, and the optimization method adopts Taguchi method.

Following parameter optimization, this paper presents the relatively optimal motor model. The optimization results are presented in Table 2, and the model parameters are detailed in Table 3. In addition, it is worth mentioning that the motor proposed in this paper has a number of parameters that affect the performance of the motor. Only the main parameters are optimized in this paper, and there is still the possibility of further optimization and improvement of the motor performance.

To evaluate the robustness of this parameter in practical applications, this study quantifies the sensitivity of motor performance to key parameters within a ±0.1 mm manufacturing tolerance range. The computational procedure is formulated in Equation (5)

$$S_j(x_i) = \frac{V(E(y_j/x_i))}{V(y_j)} \quad (i = 1, 2, 3j = 1, 2) \tag{5}$$

where x_i represents the ith design variable, which refers to w_{mt}, w_{st}, and h_s in this paper; y_j represents the jth optimization objective, which refers to F_{avg} and F_{rip} in this paper; $E(y_j/x_i)$ represents the mean value of y_j when x_i is constant; $V(E(y_j/x_i))$ represents the variance of $E(y_j/x_i)$; $V(y_j)$ represents the variance of y_j; and $S_j(x_i)$ is the sensitivity index of the ith design variable to the jth optimization objective.

The computational results are presented in Fig. 12. Overall, variations in key parameters within a small range exhibit low sensitivity to motor performance, indicating robust characteristics suitable for practical applications. Notably, the primary tooth width w_{mt} demonstrates the highest sensitivity to motor performance, requiring tighter manufacturing tolerances that are both achievable in practical manufacturing and consistent with established process requirements.

TABLE 2. The main parameters after optimization.

Items	Specifications
Primary iron core width, w (mm)	150
Air gap length, g (mm)	0.8
PM height, h_{pm} (mm)	16
Primary height, h_m (mm)	50
Primary tooth width, w_{mt}(mm)	6.3
Primary slot width, w_{ms} (mm)	8.5
PM width, w_{pm} (mm)	6.1
distance between segments, d_s (mm)	1
Secondary pole pitch, τ_s (mm)	35
Secondary tooth width, w_{st} (mm)	26.5
Secondary height, h_s (mm)	6.4
Rated speed, v (m/s)	0.5
Turns of coils per slot, N	53
Rated current, I (A)	15

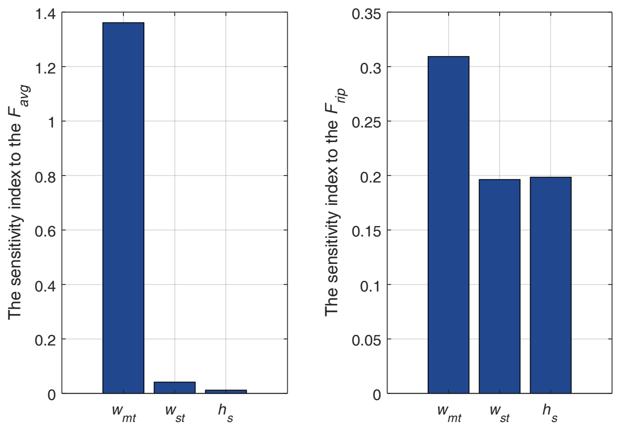

FIGURE 12. Parameter sensitivity index.

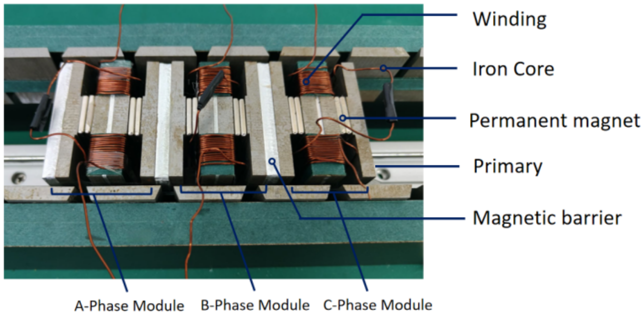

FIGURE 13. Prototype structure diagram.

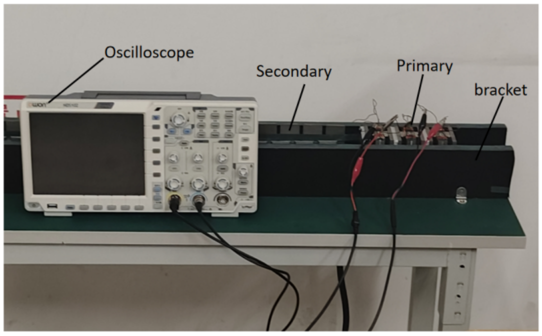

FIGURE 14. Test bench.

TABLE 3. Parameter optimization results.

Items	Initial (After structural optimization)	Parameter Optimization
F_{avg} (N)	767	774.75
F_{rip} (N)	46	42.61
F_{rip}/F_{avg}	6%	5.5%

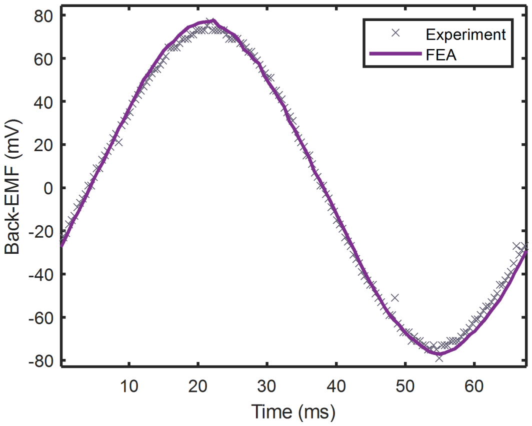

FIGURE 15. No-load back electromotive force experiment.

3.4. Performance Comparison

We compared the proposed motor with other state-of-the-art designs under the same air gap width, motor size, current amplitude, and current density, as shown in Table 4.

TABLE 4. Comparison of the proposed design with the existing design.

Items	Proposed	Ref. [14]	Ref. [26]	Ref. [13]
F_{avg} (N)	550	565	349.4	402.7
F_{rip} (N)	30.25	99.82	19.46	180
F_{rip}/F_{avg}	5.5%	17.7%	5.57%	44.7%

Compared with [14], the average thrust of the motor proposed in this paper is slightly lower, but the thrust fluctuation is significantly reduced. Compared with [26], the average thrust value is increased by 57.4% under similar thrust fluctuation. Compared with [13], both thrust fluctuation and thrust mean have been significantly improved. The secondary sectional modular bilateral flux switching linear motor proposed in this paper achieves a very low thrust fluctuation and a high mean thrust.

4. PROTOTYPE AND EXPERIMENT

The prototype has been constructed to validate the efficacy of the proposed model, as depicted in Fig. 13 and Fig. 14. The magnetic barrier material is aluminum, and all the core materials are silicon steel sheets. More detailed experimental parameters are shown in Table 5. The no-load back EMF was measured by back-driven method. The comparison of the test no-load back EMF with the simulation results is illustrated in Fig. 15.

The results indicate that the no-load back EMF exhibits favorable sinusoidal characteristics. However, there is a discrepancy in the amplitude of the back electromotive force between the experimental and simulation results. The experimen-

TABLE 5. Experimental parameters.

Items	Specifications
Primary iron core width, w (mm)	40
Air gap length, g (mm)	3.5
PM height, h_{pm} (mm)	19.4
Primary height, h_m (mm)	50
Primary tooth width, w_{mt} (mm)	6
Primary slot width, w_{ms} (mm)	8
PM width, w_{pm} (mm)	6
distance between segments, d_s(mm)	2
Secondary pole pitch, τ_s (mm)	36
Secondary tooth width, w_{st} (mm)	31
Secondary height, h_s (mm)	6
Rated speed, v (m/s)	0.53
Turns of coils per slot, N	16
Remanence, B_r (tesla)	0.52

tal result is 75 mV, while the simulation result is 77.5 mV. This difference is attributed to experimental errors and the simulation's neglect of end leakage flux. Consequently, the amplitude difference of the no-load back electromagnetic force remains within acceptable limits. In conclusion, the experimental results demonstrate good agreement with simulation outcomes, thereby validating the effectiveness of both the motor design methodology and finite element simulation approach.

5. CONCLUSION

This paper presents a novel segmented secondary modular double-sided flux-switching linear motor tailored for long-stroke linear traction applications. In comparison to existing double-side flux-switched linear motors, the proposed motor delivers higher thrust and lower thrust fluctuation in the same motor size, current amplitude, and current density. This superior thrust performance is attributed to a new primary structure, modular composition, and an effective structural optimization method based on the harmonic component of the detent force. Finally, a prototype is constructed to validate the efficacy of the proposed motor.

ACKNOWLEDGEMENT

This study was funded by the National Natural Science Foundation of China Hebei Province (grant number A2022210024).

REFERENCES

[1] Liu, J., L. Shi, K. Guo, *et al.*, "Suppression of force fluctuations in segmented PMLSM using harmonic injection during phase open of the inverter," *Proceedings of the CSEE*, Vol. 44, No. 13, 5308–5318, 2024.

[2] Hu, D., W. Xu, R. Dian, Y. Liu, and J. Zhu, "Loss minimization control of linear induction motor drive for linear metros," *IEEE Transactions on Industrial Electronics*, Vol. 65, No. 9, 6870–6880, 2017.

[3] Cheng, M., P. Han, Y. Du, H. Wen, and X. Li, "A tutorial on general air-gap field modulation theory for electrical machines," *IEEE Journal of Emerging and Selected Topics in Power Electronics*, Vol. 10, No. 2, 1712–1732, 2021.

[4] Su, P., W. Hua, Z. Wu, P. Han, and M. Cheng, "Analysis of the operation principle for rotor-permanent-magnet flux-switching machines," *IEEE Transactions on Industrial Electronics*, Vol. 65, No. 2, 1062–1073, 2017.

[5] Zhu, Y., Y. Li, Y. Chang, J. Li, and J. Chen, "Comparative analysis of normal force characteristics and dynamic influence of linear flux-switching permanent magnet motor for rail transit," *IEEE Access*, Vol. 12, 132 409–132 420, 2024.

[6] Du, Y., X. Yan, L. Zhang, X. Zhu, Y. Mao, and X. Sun, "Fault-tolerant SVPWM strategy of dual-three-phase linear flux-switching permanent magnet motor based on virtual voltage vector," *Proceedings of the CSEE*, Vol. 44, No. 3, 1153–1161, 2024.

[7] Lu, Q. and Y. Shen, "Overview of permanent magnet linear machines with primary excitation," in *2021 Sixteenth International Conference on Ecological Vehicles and Renewable Energies (EVER)*, 1–7, Monte-Carlo, Monaco, May 2021.

[8] Cao, R., M. Lu, N. Jiang, and M. Cheng, "Comparison between linear induction motor and linear flux-switching permanent-magnet motor for railway transportation," *IEEE Transactions on Industrial Electronics*, Vol. 66, No. 12, 9394–9405, 2019.

[9] Cao, R., M. Cheng, C. Mi, W. Hua, and W. Zhao, "Comparison of complementary and modular linear flux-switching motors with different mover and stator pole pitch," *IEEE Transactions on Magnetics*, Vol. 49, No. 4, 1493–1504, 2012.

[10] Cao, R., E. Su, and X. Zhang, "Investigation of linear flux-switching permanent magnet motor with segmented secondary for rail transit," *Transactions of China Electrotechnical Society*, Vol. 35, No. 5, 1001–1012, 2020.

[11] Zhou, Y., C. Shi, R. Qu, D. Li, and Y. Gao, "Overview of flux-modulation linear permanent magnet machines," *Proceedings of the CSEE*, Vol. 44, No. 4, 1469–1484, 2021.

[12] Cheng, M., B. Zhang, S. Wang, and W. Wang, "Modular thin yoke linear flux-switching permanent magnet machine and control system," *Journal of Electrical Engineering*, Vol. 16, No. 1, 1–8, 2021.

[13] Zhao, Q., C. Wen, X. Zhao, M. Li, K. Lv, and X. Wang, "Optimal design of double-sided linear flux switching permanent magnet motor," *Progress In Electromagnetics Research M*, Vol. 110, 39–48, 2022.

[14] Ullah, B., F. Khan, S. Hussain, and B. Khan, "Modeling, optimization, and analysis of segmented stator flux switching linear hybrid excited machine for electric power train," *IEEE Transactions on Transportation Electrification*, Vol. 8, No. 3, 3546–3553, 2022.

[15] Shafiei, S., T. Sharifi, M. A. N. Dehdez, and M. Bagheri, "A modified partitioned-stator flux-switching permanent magnet machine for enhancing torque-density in electric vehicle powertrains," *IET Electric Power Applications*, Vol. 19, No. 1, e70000, 2025.

[16] Badewa, O. A., A. Mohammadi, D. D. Lewis, S. Essakiappan, M. Manjrekar, and D. M. Ionel, "Electromagnetic design characterization of synchronous machines with flux switching effect employing reluctance rotors and stators with PMs and AC concentrated coils," *IEEE Transactions on Industry Applications*, 2025.

[17] Liu, C., D. Xu, W. Wu, and B. Yang, "Research on a novel flux-switching permanent magnet motor with adjustable torque ripple using an auxiliary rotor," *Machines*, Vol. 12, No. 12, 929, 2024.

[18] Wang, P., W. Hua, G. Zhang, B. Wang, and M. Cheng, "Principle of flux-switching permanent magnet machine by magnetic field modulation theory part I: Back-electromotive-force generation," *IEEE Transactions on Industrial Electronics*, Vol. 69, No. 3, 2370–2379, 2021.

[19] Wang, D., G. Guang, B. Wang, W. Feng, and X. Wang, "Research on a novel stator concentrated-flux ferrite permanent magnetic flux switching motor," *Proceedings of the CSEE*, 2024.

[20] Ling, Z., Y. Gu, W. Zhao, J. Ji, and Y. Zeng, "Topology evolution and torque improvement mechanism of magnetic field modulated machine based on energy analysis method," *Proceedings of the CSEE*, 2024.

[21] Wang, P., W. Hua, M. Hu, Z. Zhang, Y. Wang, and M. Cheng, "Design and performance analysis of flux-switching permanent magnet machine with cos-chamfering rotor," *Proceedings of the CSEE*, Vol. 42, No. 22, 8372–8381, 2022.

[22] Wang, H., *et al.*, "Research on slot/pole number combinations selection for high suspension performance bearingless permanent magnet slice motor based on elimination of coupled harmonics," *Proceedings of the CSEE*, 2024.

[23] Wang, Y. and S. Wang, "Analysis and compensation of eccentric unbalanced magnetic pulling force in bearingless permanent magnet slice motors based on magnetic field," *Transactions of China Electrotechnical Society*, 2024.

[24] Li, Y., Q. Zhou, S. Ding, *et al.*, "Investigation of air-gap field modulation effect on V-shaped consequent-pole permanent magnet synchronous machines," *Proceedings of the CSEE*, Vol. 44, No. 5, 2019–2026, 2024.

[25] Cheng, M., P. Han, and W. Hua, "General airgap field modulation theory for electrical machines," *IEEE Transactions on Industrial Electronics*, Vol. 64, No. 8, 6063–6074, 2017.

[26] Liu, C.-T., C.-C. Hwang, P.-L. Li, S.-S. Hung, and P. Wendling, "Design optimization of a double-sided hybrid excited linear flux switching PM motor with low force ripple," *IEEE Transactions on Magnetics*, Vol. 50, No. 11, 1–4, 2014.